Commun. Comput. Phys.
doi: 10.4208/cicp.scpde14.14s

Vol. 19, No. 5, pp. 1265-1286
May 2016

A Numerical Study of Complex Reconstruction in Inverse Elastic Scattering

Guanghui Hu[1], Jingzhi Li[2,*], Hongyu Liu[3] and Qi Wang[4]

[1] *Beijing Computational Science Research Center, Beijing 100094, P.R. China.*
[2] *Department of Mathematics, Southern University of Science and Technology, Shenzhen 518055, P.R. China.*
[3] *Department of Mathematics, Hong Kong Baptist University, Kowloon Tong, Hong Kong.*
[4] *Department of Computing Sciences, School of Mathematics and Statistics, Xi'an Jiaotong University, Xi'an, 710049, P.R. China.*

Received 16 January 2015; Accepted 26 June 2015

Abstract. The purpose of this paper is to numerically realize the inverse scattering scheme proposed in [19] of reconstructing complex elastic objects by a single far-field measurement. The unknown elastic scatterers might consist of both rigid bodies and traction-free cavities with components of multiscale sizes presented simultaneously. We conduct extensive numerical experiments to show the effectiveness and efficiency of the imaging scheme proposed in [19]. Moreover, we develop a two-stage technique, which can significantly speed up the reconstruction to yield a fast imaging scheme.

AMS subject classifications: 74J20, 74J25, 35Q74, 35R30

Key words: Inverse elastic scattering, complex scatterers, cavities and rigid elastic bodies, single-shot method.

1 Introduction

This work concerns the numerical realization of an imaging scheme proposed in [19] for reconstructing complex elastic scatterers embedded in a homogeneous isotropic background medium occupying $\mathbb{R}^3$. Let λ and μ be two constants such that $\mu>0$ and $3\lambda+2\mu>0$. λ and μ are the Lamé constants that constitute the parameterization of the background elastic material. Throughout, we assume that the density of the background elastic medium is normalized to be 1. Let $D\subset\mathbb{R}^3$ be a bounded domain with a C^2 boundary ∂D and a connected complement $\mathbb{R}^3\backslash\overline{D}$. D denotes the inhomogeneous elastic body

---

[*] Corresponding author. *Email addresses:* `hu@csrc.ac.cn` (G. Hu), `li.jz@sustc.edu.cn` (J. Li), `hongyu.liuip@gmail.com` (H. Liu), `qi.wang.xjtumath@gmail.com` (Q. Wang)

that we intend to recover by using elastic wave measurements made away from it. In what follows, D is referred to as a *scatterer*. The detecting elastic field is taken to be the time-harmonic plane wave of the form

$$u^{in}(x)=u^{in}\left(x;d,d^{\perp},\alpha,\beta,\omega\right)=\alpha d e^{\mathrm{i}k_p x\cdot d}+\beta d^{\perp}e^{\mathrm{i}k_s x\cdot d},\quad \alpha,\beta\in\mathbb{C}, \tag{1.1}$$

where $d\in\mathbb{S}^2:=\left\{x\in\mathbb{R}^3:|x|=1\right\}$ is the incident direction ; the vector $d^{\perp}\in\mathbb{S}^2$ satisfying $d^{\perp}\cdot d=0$ denotes the polarization direction; and $k_s:=\omega/\sqrt{\mu}$, $k_p:=\omega/\sqrt{\lambda+2\mu}$ denote the shear and compressional wave numbers, respectively. Let $u^{sc}(x)\in\mathbb{C}^3$, $x\in\mathbb{R}^3\backslash\overline{D}$ denote the perturbed/scattered elastic displacement field caused by the elastic scatterer and $u:=u^{in}+u^{sc}$ denote the total field. The propagation of the elastic field is governed by the following reduced Navier equation (or Lamé system)

$$(\triangle^*+\omega^2)u=0\quad\text{in }\mathbb{R}^3\backslash\overline{D},\quad \triangle^*:=\mu\triangle+(\lambda+\mu)\text{grad div}. \tag{1.2}$$

In order to complete the description of the direct elastic scattering problem, we next prescribe the physically meaningful boundary conditions satisfied by the elastic field on ∂D and at the infinity.

Define the infinitesimal strain tensor by

$$\epsilon(u):=\frac{1}{2}\left(\nabla u+\nabla u^T\right)\in\mathbb{C}^{3\times 3}, \tag{1.3}$$

where ∇u and ∇u^T stand for the Jacobian matrix of u and its adjoint, respectively. By Hooke's law the Cauchy stress tensor relates to the strain tensor via the identity

$$\sigma(u)=\lambda(\text{div}\,u)\mathbf{I}+2\mu\epsilon(u)\in\mathbb{C}^{3\times 3}, \tag{1.4}$$

where $\mathbf{I}$ denotes the 3×3 identity matrix. The surface traction (or the stress operator) on ∂D is defined as

$$Tu=T_{\nu}u:=\nu\cdot\sigma(u)=(2\mu\nu\cdot\text{grad}+\lambda\nu\text{div}+\mu\nu\times\text{curl})u, \tag{1.5}$$

where ν denotes the unit normal vector to ∂D pointing into $\mathbb{R}^3\backslash\overline{D}$. We also define $Ru:=u$ in the following. If D is a cavity, then one has the traction-free boundary condition $Tu=0$ on ∂D; and if D is a rigid body, then one has $Ru=0$ on ∂D.

Decomposing the incident wave u^{in} in (1.1), we denote by $u_p^{in}:=de^{\mathrm{i}k_p x\cdot d}$ the (normalized) *plane pressure wave*, and $u_s^{in}:=d^{\perp}e^{\mathrm{i}k_s x\cdot d}$ the (normalized) *plane shear wave*. By Hodge decomposition, the scattered field u^{sc} can be decomposed into

$$u^{sc}:=u_p^{sc}+u_s^{sc},\quad u_p^{sc}:=-\frac{1}{k_p^2}\text{grad div}u^{sc},\quad u_s^{sc}:=\frac{1}{k_s^2}\text{curl curl}u^{sc},$$

where the vector functions u_p^{sc} and u_s^{sc} are referred to as the pressure (P) and shear (S) parts of u^{sc}, respectively, satisfying

$$
\begin{aligned}
&(\triangle+k_p^2)u_p^{sc}=0, \quad \mathrm{curl}\,u_p^{sc}=0 \quad \text{in } \mathbb{R}^3\backslash\overline{D},\\
&(\triangle+k_s^2)u_s^{sc}=0, \quad \mathrm{div}\,u_s^{sc}=0 \quad \text{in } \mathbb{R}^3\backslash\overline{D}.
\end{aligned}
$$

The scattered field u^{sc} satisfies the *Kupradze's radiation condition* in the sense that

$$
\lim_{r\to\infty}\left(\frac{\partial u_p^{sc}}{\partial r}-\mathrm{i}k_p u_p^{sc}\right)=0, \quad \lim_{r\to\infty}\left(\frac{\partial u_s^{sc}}{\partial r}-\mathrm{i}k_s u_s^{sc}\right)=0, \quad r=|x|, \tag{1.6}
$$

uniformly in all directions $\hat{x}=x/|x|\in\mathbb{S}^2$.

The direct scattering system described above is well understood (see e.g., [23]). Corresponding to u_p^{sc} and u_s^{sc}, the radiation conditions in (1.6) lead to the far-field patterns u_p^∞ and u_s^∞, which can be read off from the following asymptotics

$$
u^{sc}(x)=\frac{\exp(ik_p|x|)}{4\pi(\lambda+\mu)|x|}u_p^\infty(\hat{x})+\frac{\exp(\mathrm{i}k_s|x|)}{4\pi\mu|x|}u_s^\infty(\hat{x})+\mathcal{O}\left(\frac{1}{|x|^2}\right), \quad |x|\to\infty. \tag{1.7}
$$

Based on $u_p^\infty(\hat{x})$ and $u_s^\infty(\hat{x})$, we define the full far-field pattern u^∞ of u^{sc} as

$$
u^\infty(\hat{x}):=u_p^\infty(\hat{x})+u_s^\infty(\hat{x}). \tag{1.8}
$$

In [19] we proposed several imaging schemes to reconstruct a cavity or a rigid elastic body by knowledge of $u_p^\infty(\hat{x})$, $u_s^\infty(\hat{x})$ or $u^\infty(\hat{x})$, corresponding to a single incident plane wave u^{in} in (1.1) with fixed α,β, $d,d^\perp$ and k_p,k_s. The aim of this paper is to conduct extensive numerical experiments to show the effectiveness and efficiency of the developed inversion schemes. In what follows, we shall write $u_p^\infty(\hat{x},D)$, $u_s^\infty(\hat{x},D)$ or $u^\infty(\hat{x},D)$ to signify the dependence on the scatterer D. In the present study, the scatterer D could be very general, which may consist of multiple components, and each component is either rigid or traction-free. Moreover, there might be scatterer components of multiscale sizes presented simultaneously.

The rest of the paper is organized as follows. In Sections 2 and 3, we briefly discuss the schemes, respectively, of recovering multiple small and regular-size scatterers and then present the corresponding numerical examples. Section 4 is devoted to the numerical reconstruction of multiscale scatterers. In Section 5, we present the two-stage technique which can yield a fast imaging scheme.

2 Reconstructing multiple small scatterers

In this section, we consider the reconstruction of multiple small scatterers. Throughout the rest of the paper, we assume that $\omega\sim 1$. That is, the wavelength of the elastic waves is given by $2\pi/\omega\sim 1$ and hence the size of a scatterer can be expressed in terms of its Euclidean diameter.

We first introduce the class of small scatterers for our study. Let $l_s\in\mathbb{N}$ and $D_j\subset\mathbb{R}^3, 1\leq j\leq l_s$ be bounded simply-connected C^2 domains containing the origin. For $\rho\in\mathbb{R}_+$, we introduce a scaling operator

$$\Lambda_\rho D_j := \{\rho x; x\in D_j\} \tag{2.1}$$

and set

$$\Omega_j^{(s)} = z_j + \Lambda_\rho D_j, \quad z_j\in\mathbb{R}^3, \quad 1\leq j\leq l_s, \tag{2.2}$$

where each $\Omega_j^{(s)}$ is referred to as a scatterer component. The parameter $\rho_j\in\mathbb{R}_+$ represents the relative size of the scatterer (or, more precisely, each of its components). Then a scatterer component $\Omega_j^{(s)}$ is said to be *small* if $\rho\ll 1$. For a collection of small scatterers, we set

$$\Omega^{(s)} := \bigcup_{j=1}^{l_s}\Omega_j^{(s)}. \tag{2.3}$$

$\Omega^{(s)}$ is called a *multiple small scatterer* if $l_s>1$ and the following qualitative sparsity assumption is satisfied

$$L_s := \mathrm{dist}(z_i,z_j)\gg 1 \quad \text{for } i\neq j,\ 1\leq i,j\leq l_s. \tag{2.4}$$

In order to recover the multiple scatterers in $\Omega^{(s)}$ in (2.3), the following three imaging functionals are proposed in [19],

$$I_1(z) = \frac{1}{\left\|u_p^\infty(\hat{x},\Omega^{(s)})\right\|_{L^2}^2}\sum_{n=0}^{1}\sum_{m=-n}^{n}\sum_{l=1}^{3}\left|\left\langle u_p^\infty(\hat{x},\Omega^{(s)}),(\hat{x}\otimes\hat{x})Y_n^m(\hat{x})\mathbf{e}_l e^{-\mathrm{i}k_p\hat{x}\cdot z}\right\rangle\right|^2, \tag{2.5}$$

$$I_2(z) = \frac{1}{\left\|u_s^\infty(\hat{x},\Omega^{(s)})\right\|_{L^2}^2}\sum_{n=0}^{1}\sum_{m=-n}^{n}\sum_{l=1}^{3}\left|\left\langle u_s^\infty(\hat{x},\Omega^{(s)}),(\hat{x}\otimes\hat{x})Y_n^m(\hat{x})\mathbf{e}_l e^{-\mathrm{i}k_s\hat{x}\cdot z}\right\rangle\right|^2, \tag{2.6}$$

$$I_3(z) = \frac{1}{\left\|u^\infty(\hat{x},\Omega^{(s)})\right\|_{L^2}^2}\sum_{n=0}^{1}\sum_{m=-n}^{n}\sum_{l=1}^{3}|f_{n,m,l}(z)|^2, \tag{2.7}$$

where $z\in\mathbb{R}^3$ and

$$f_{n,m,l}(z) := \left\langle u^\infty(\hat{x};\Omega^{(s)}), \left[(\hat{x}\otimes\hat{x})e^{-\mathrm{i}k_p\hat{x}\cdot z} + (\mathbf{I}-\hat{x}\otimes\hat{x})e^{-\mathrm{i}k_s\hat{x}\cdot z}\right]Y_n^m(\hat{x})\mathbf{e}_l\right\rangle.$$

Here and in what follows, the notation $\langle\cdot,\cdot\rangle$ denotes the inner product in $L^2 := L^2\left(\mathbb{S}^2\right)^3$ with respect to the variable $\hat{x}\in\mathbb{S}^2$, defined as $\langle\mathbf{u},\mathbf{v}\rangle := \int_{\mathbb{S}^2}\mathbf{u}(\hat{x})\cdot\overline{\mathbf{v}(\hat{x})}ds(\hat{x})$. In (2.5)-(2.7), the constant vectors $\mathbf{e}_l$, $1\leq l\leq 3$ are the standard Euclidean base vectors in $\mathbb{R}^3$ and $Y_n^m(\hat{x})$,

---

Algorithm 1 Locating multiple small scatterers $\Omega^{(s)}$ in (2.3) with I_m, $m=1,2,3$.

Step 1 For an unknown scatterer $\Omega^{(s)}$ with multiple components in (2.3), collect $u_p^\infty(m=1)$, $u_s^\infty(m=2)$, $u^\infty(m=3)$ by sending a single detecting plane wave (1.1).

Step 2 Select a sampling region with a mesh $\mathcal{T}_h$ containing $\Omega^{(s)}$.

Step 3 For each sampling point $z\in\mathcal{T}_h$, calculate I_m according to the measurement data.

Step 4 Locate all the local maximizers of $I_m(z)$ on $\mathcal{T}_h$, which represent locations of the scatterer components of $\Omega^{(s)}$.

$n=0,1,\cdots$, $m=-n,\cdots,n$, are the spherical harmonics (cf. [11]). The imaging functionals $I_m(z)$, $m=1,2,3$, possess a certain local maximum behavior which can be used to locate the scatterer components of $\Omega^{(s)}$, namely z_j, $1\leq j\leq l_s$. To be more specific, the values of $I_m(z)\,(m=1,2,3)$ would become larger when approaching each $z_j\,(1\leq j\leq l_s)$, and be close to zero when z is far away from each $z_j\,(1\leq j\leq l_s)$. Here, we would like to note that $k_s/k_p=\sqrt{(\lambda+2\mu)/\mu}$, and hence $k_s>k_p$ if $\lambda>0$. Generically, one would have $\lambda>0$, and therefore, one can expect that the imaging functionals I_2 and I_3 would produce better reconstructions than the imaging functional I_1. This is actually numerically confirmed in our experiments. The scheme for locating the multiple small scatterers is formulated as Algorithm 1.

We proceed to present a numerical example to illustrate the effectiveness of Algorithm 1. Throughout the rest of the paper, for the numerical examples, the synthetic far-field data are obtained by computing the corresponding direct elastic scattering problem. To be more specific, we solve the Lamé system (1.2) by the standard Finite Element Method (FEM), where the unbounded computed region is truncated by the Perfect Matched Layers (PMLs). Furthermore, we have refined the mesh several times until a sufficiently accurate solution is achieved. Then the P-part and S-part far-field could be directly derived by implementing

$$u_p^\infty(\hat{x})=\frac{k_p^2}{4\pi\omega^2}\int_{\partial D}[T_{\nu(y)}\hat{x}\hat{x}^Te^{-\mathrm{i}k_p\hat{x}\cdot y}]^Tu(y)-\hat{x}\hat{x}^Te^{-\mathrm{i}k_p\hat{x}\cdot y}T_{\nu(y)}u(y),\quad \hat{x}\in\Omega, \tag{2.8}$$

and

$$u_s^\infty(\hat{x})=\frac{k_s^2}{4\pi\omega^2}\int_{\partial D}[T_{\nu(y)}[\mathbf{I}-\hat{x}\hat{x}^T]e^{-\mathrm{i}k_s\hat{x}\cdot y}]^Tu(y)-[\mathbf{I}-\hat{x}\hat{x}^T]e^{-\mathrm{i}k_s\hat{x}\cdot y}T_{\nu(y)}u(y),\quad \hat{x}\in\Omega, \tag{2.9}$$

respectively. Unless otherwise stated, we always collect the far-field pattern $u^\infty(\hat{x}_i)\,(i=1,\cdots,590)$ on 590 Lebdev quadrature points, which is important in evaluating the integral in the indicator functions. And to show the stability of the locating scheme, we have also added a 5% Gaussian noise on the obtained far-field data. That is,

$$u^{\infty}_{\tau,\text{noise}}(\hat{x}_i)=u^{\infty}_{\tau}(\hat{x}_i)+0.05\xi\max_{i}|u^{\infty}_{\tau}(\hat{x}_i)|,\quad \tau=s,p\,\text{or}\,\emptyset, \tag{2.10}$$

where ξ obeys a gaussian distribution with expectation 0 and variance 1.

Example 2.1. Let a multiple small scatterer consist of three different components, i.e., $\Omega^{(s)}=\cup_{j=1}^{3}\Omega_j^{(s)}$, which is illustrated in Fig. 1. Here, $\Omega_1^{(s)}$ is a rigid ball located at $(-2,0,0)$, whose radius is 0.01; $\Omega_2^{(s)}$ is a traction-free ellipsoid located at $(2,0,-1.5)$, the lengths of whose semi-principal axes are 0.2, 0.2, 0.1, respectively; $\Omega_3^{(s)}$ is a traction-free cube of side length 0.2 located at $(0,0,1)$. Moreover, we set $\lambda=2$ and $\mu=1$. Impinge an incident wave of the form (1.1) with $\omega=2\pi$, $d=(1,0,0)$, $\alpha=1$ and $\beta=0$, then we collect the corresponding far-field $u^{\infty}(\hat{x})$ on the unit sphere $\mathbb{S}^1$.

From $k_s=\omega/\sqrt{\mu}$, $k_p=\omega/\sqrt{\lambda+2\mu}$ we have $k_s=2\pi$ and $k_p=\pi$. We present the slice $y=0$ of I_m $(m=1,2,3)$ in Fig. 2. It is clear that all of the three imaging functionals correctly locate

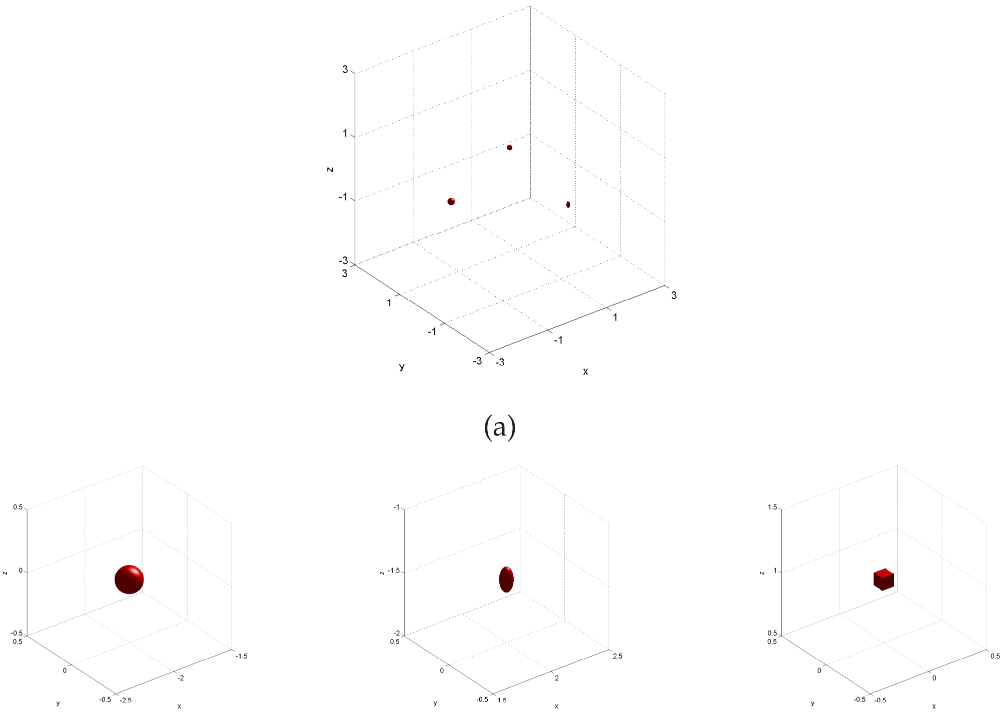

(a)

(a) (b) (c)

Figure 1: Locating multiple small scatterers. (a) The true scatterer with 3 components; (b) The true scatterer component 1 (a rigid ball); (c) The true scatterer component 2 (a traction-free ellipsoid); (b) The true scatterer component 3 (a traction-free cube).

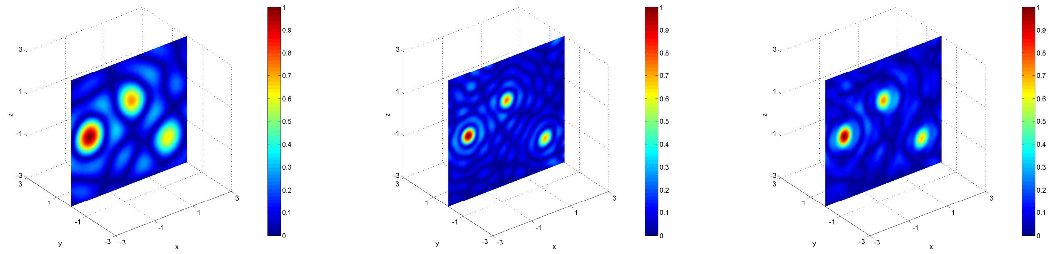

(a) (b) (c)

Figure 2: Locating multiple small scatterers. (a) The configuration of $I_1(z)$; (b) The configuration of $I_2(z)$; (c) The configuration of $I_3(z)$.

the unknown scatterer components. In addition, the decay speed is faster in Fig. 2(b) and (c) than that in Fig. 2(a), which verifies our expectation made earlier.

3 Reconstructing multiple extended scatterers

In this section, we consider locating multiple extended elastic scatterers with a single incident plane wave. Reconstructing a general elastic scatterer with a single far-field measurement is known to be a challenging issue, both theoretically and numerically. In order to overcome the difficulties involved with the generality and complexity of the scatterers, the scheme mentioned in this work requires some a priori knowledge about the target scatterers. That is, we assume that the shape of the unknown scatterer components is confined by a *base scatterer class*. With this assumption, we try to find some information on the scatterers, e.g., the location, size, and rotation degree.

Let us first describe the *base scatterer class* and the *multiple extended scatterers*. For $l' \in \mathbb{N}_+$, let $\Sigma_j \subset \mathbb{R}^3 (1 \le j \le l')$ be a bounded simply-connected C^2 domain containing the origin. Then we define

$$\mathcal{A} := \{\Sigma_j\}_{j=1}^{l'}, \quad l' \in \mathbb{N}. \tag{3.1}$$

Here $\mathcal{A}$ is said to be a *base scatterer class*; each *base scatterer* $\Sigma_j, 1 \le j \le l'$, could be either rigid or traction-free. Moreover, throughout this study we would always assume that $\operatorname{diam}(\Sigma_j) \sim 1$.

Let $l_e \in \mathbb{N}$ denote the number of the unknown scatterer components. For $j = 1, 2, \cdots, l_e$, set $r_j \in \mathbb{R}_+$ such that

$$r_j \in [R_0, R_1], \quad 0 < R_0 < R_1 < +\infty, \quad R_0 \sim \mathcal{O}(1),$$

and moreover, let $(\theta_j, \phi_j, \psi_j) \in [0, 2\pi]^2 \times [0, \pi], j = 1, 2, \cdots, l_e$ be l_e Euler angles. Define the scaling operator Λ_{r_j} to be the same as the one given in (2.1). Denote by $\mathcal{R}_j := \mathcal{R}(\theta_j, \phi_j, \psi_j) \in$

$SO(3)$ the 3D rotation matrix around the origin whose Euler angles are $\theta_j\in[0,2\pi]$, $\phi_j\in[0,2\pi]$ and $\psi_j\in[0,2\pi]$; and define $\mathcal{R}_j\Sigma:=\{\mathcal{R}_jx: x\in\Sigma,\Sigma\in\mathcal{A}\}$. For $z_j\in\mathbb{R}^3$, we let

$$\Omega^{(e)}=\bigcup_{j=1}^{l_e}\Omega_j^{(e)},\quad \Omega_j^{(e)}:=z_j+\mathcal{R}_j\Lambda_{r_j}\Sigma_j,\quad \Sigma_j\in\mathcal{A}, \tag{3.2}$$

where $\Omega^{(e)}$ is said to be the *multiple extended scatterers* in the current study. Obviously, $\Omega^{(e)}$ is a collection of scatterer components $\Omega_j^{(e)}$ that obtained by scaling, rotating and translating Σ_j with the parameters r_j, (θ_j,ϕ_j,ψ_j) and z_j, respectively. In the sequel, the parameter z_j, Euler angles (θ_j,ϕ_j,ψ_j), number r_j and the reference scatterer Σ_j will be respectively referred to as the *position*, *orientation*, *size* and *shape* of the scatterer component $\Omega_j^{(e)}$ in $\Omega^{(e)}$. To reduce the multiple sampling effect, we also impose the following sparsity assumption on the extended scatterer,

$$L_e=\min_{j\neq j',1\leq j,j'\leq l_e}\operatorname{dist}(\Omega_j^{(e)},\Omega_{j'}^{(e)})\gg 1. \tag{3.3}$$

Next, we introduce the h-net ($h\in\mathbb{R}_+$, $h\ll 1$) for the base scatterer class $\mathcal{A}$. Let $\mathcal{N}_1$ be a suitably chosen finite index set such that $\{\mathcal{R}_j\}_{j\in\mathcal{N}_1}=\{R(\theta_j,\phi_j,\psi_j)\}_{j\in\mathcal{N}_1}$ is an h-net of $SO(3)$. That is, for any rotation matrix $\mathcal{R}\in SO(3)$, there exists $j\in\mathcal{N}_1$ such that $\|\mathcal{R}_j-\mathcal{R}\|\leq h$. For a simply-connected domain Σ_h containing the origin, we define

$$\mathcal{R}_h\Sigma:=\{\mathcal{R}_j\Sigma\}_{j\in\mathcal{N}_1}. \tag{3.4}$$

In a similar manner, for Λ_r with $r\in[R_0,R_1]$, we let $\mathcal{N}_2$ be a suitably chosen finite index set such that $\{r_j\}_{j\in\mathcal{N}_2}$ is an h-net of $[R_0,R_1]$. Define

$$\Lambda_h\Sigma:=\{\Lambda_{r_j}\Sigma\}_{j\in\mathcal{N}_2}. \tag{3.5}$$

Then we augment the admissible reference space $\mathcal{A}$ to be

$$\mathcal{A}_h=\mathcal{R}_h\Lambda_h\mathcal{A}=\bigcup_{j=1}^{l'}\{\mathcal{R}_h\Lambda_h\Sigma_j\}:=\{\widetilde{\Sigma}_j\}_{j=1}^{l''}, \tag{3.6}$$

where l'' denotes the cardinality of the discrete set $\mathcal{A}_h$. Indeed, $\mathcal{A}_h$ can be taken as an h-net of $\mathcal{A}$ in the sense that for any $\Sigma\in\mathcal{A}$, there exists $\widetilde{\Sigma}\in\mathcal{A}_h$ such that $d_H(\overline{\Sigma},\overline{\widetilde{\Sigma}})\leq Ch$, where d_H denotes the Hausdorff distance and C is a positive constant depending only on $\mathcal{A}$. For the augmented admissible reference space $\mathcal{A}_h$, two assumptions should be made:

(i) $u_\tau^\infty(\hat{x},\widetilde{\Sigma}_j)\neq u_\tau^\infty$ for $\tau=s,p\text{or}\emptyset$, and $j\neq j',1\leq j,j'\leq l''$.

(ii) $\left\|u_\tau^\infty(\hat{x},\widetilde{\Sigma}_j)\right\|_{L^2}\geq\left\|u_\tau^\infty(\hat{x},\widetilde{\Sigma}_{j'})\right\|_{L^2}$ for $\tau=s,p,\text{or}\emptyset$, and $j<j',1\leq j,j'\leq l''$.

Assumption (i) states that one can uniquely determine an elastic scatterer by using a single far-field pattern, which is a well-known conjecture in the inverse scattering theory. Since $\mathcal{A}_h$ is known, assumption (i) can be verified in advance. Assumption (ii) gives the recovered order of the scatterer components, which can be fulfilled by reordering the elements in $\mathcal{A}_h$ if necessary.

For an incident plane wave of the form (1.1) with $\alpha=1$, $\beta=0$ or $\alpha=0$, $\beta=1$, we introduce the following indicator functions,

$$W_1^j(z)=\frac{\left|\left\langle u_p^\infty(\hat{x};\Omega^{(m)}), A_1^j(\hat{x};z)\right\rangle\right|}{\|u_p^\infty(\hat{x},\Omega_j^{(e)})\|_{L^2}^2}, \quad z\in\mathbb{R}^3, \tag{3.7}$$

$$W_2^j(z)=\frac{\left|\left\langle u_s^\infty(\hat{x};\Omega^{(m)}), A_2^j(\hat{x};z)\right\rangle\right|}{\|u_s^\infty(\hat{x},\Omega_j^{(e)})\|_{L^2}^2}, \quad z\in\mathbb{R}^3, \tag{3.8}$$

$$W_1^j(z)=\frac{\left|\left\langle u^\infty(\hat{x};\Omega^{(m)}), A_1^j(\hat{x};z)+A_2^j(\hat{x};z)\right\rangle\right|}{\|u^\infty(\hat{x},\Omega_j^{(e)})\|_{L^2}^2}, \quad z\in\mathbb{R}^3, \tag{3.9}$$

where for $j=1,2,\cdots,l_e$,

$$A_1^j(\hat{x},z):=e^{\mathrm{i}k_p(d-\hat{x})\cdot z}u_p^\infty(\hat{x};d,d^\perp,\alpha,0,\Omega_j^{(e)})+e^{\mathrm{i}(k_sd-k_p\hat{x})\cdot z}u_p^\infty(\hat{x};d,d^\perp,0,\beta,\Omega_j^{(e)}),$$

and

$$A_2^j(\hat{x},z):=e^{\mathrm{i}(k_pd-k_s\hat{x})\cdot z}u_s^\infty(\hat{x};d,d^\perp,\alpha,0,\Omega_j^{(e)})+e^{\mathrm{i}k_s(d-\hat{x})\cdot z}u_s^\infty(\hat{x};d,d^\perp,0,\beta,\Omega_j^{(e)}).$$

In what follows, the indicator functions (3.7)-(3.9) shall be adopted to locate extended scatterers. Since $\Sigma_j\in\mathcal{A}$ is known in advance, $W_m^j\,(m=1,2,3)$ could be understood as the projection of the scattering measurement data into a space generated by the scattering data from the admissible base scatterers. When the sampling point is at the location of the targets, i.e., $z=z_j$, the term involved z_j would be eliminated in the implementation of the indicators. Thus $W_m^j\,(m=1,2,3)$ also possesses a local maximum behavior, similar to (2.5)-(2.7). We formulate the scheme for reconstructing multiple extended scatterers in Algorithm 2.

Next, we show the indicating properties of the indicator functions for multiple extended scatterers by a numerical example.

Example 3.1. Let the base scatterer class $\mathcal{A}$ consist of two base scatterers Σ_1 and Σ_2, where Σ_1 is a traction-free ball of radius 1, and Σ_2 is a rigid 3D-kite, given in Fig. 3. The 2D-kite is a typical shape in inverse scattering experiments, whose parameter function is as follows,

$$\begin{cases} x=\cos(t)+0.65\cos(2t)-0.65, \\ y=1.5\sin(t), \end{cases} \qquad 0\le t\le 2\pi.$$

Algorithm 2 Locating multiple extended scatterers $\Omega^{(m)}$ with W_m, $m=1,2,3$.

```
Step 1  For the admissible reference scatterer class $\mathcal{A}$ in (3.1), formulate the augmented admissible $A_h$ in (3.6);
Step 2  Collect in advance the P-part ($m=1$), S-part ($m=2$) or the full far-field data ($m=3$) associated with the admissible reference scatterer class $\mathcal{A}_h$ corresponding to a single incident plane wave of the form (1.1). Reorder $\mathcal{A}_h$ if necessary to make it satisfy assumption (ii), and also verify the generic assumption (i);
Step 3  For an unknown scatterer $\Omega^{(e)}$ in (3.2), collect the P-part, S-part or the full far-field data by sending the same detecting plane wave;
Step 4  Select a sampling region with a mesh $\mathcal{T}_h$ containing $\Omega^{(e)}$;
Step 5  Set $j=1$;
Step 6  For each sampling point $z\in\mathcal{T}_h$, calculate $W_m^j(z)\,(m=1,2,3)$ according to available far-field data for $\Omega^{(e)}$;
Step 7  Locate all those significant local maximum points of $W_m^j(z)$ satisfying $W_m^j(z)\approx 1$ for the scatterer components of the form $z+\widetilde{\Sigma}_j$. Let $z_\eta$, $\eta=1,\cdots,\eta_0$ be the local maximum points found this step;
Step 8  Remove all those $z+\widetilde{\Sigma}_j$ found in Step 6 from the mesh $\mathcal{T}_h$;
Step 9  Update the far-field patterns according to the following formulae
            $u_p^{\infty,new}=u_p^\infty(\hat{x};d,d^\perp,\alpha,\beta,\Omega^{(e)})-u_p^\infty(\hat{x};d,d^\perp,\alpha,0,\widetilde{\Sigma}_j)\sum_{\eta=1}^{\eta_0}e^{\mathrm{i}k_p(d-\hat{x})\cdot z_\eta}$
                $-u_p^\infty(\hat{x};d,d^\perp,0,\beta,\widetilde{\Sigma}_j)\sum_{\eta=1}^{\eta_0}e^{\mathrm{i}(k_sd-k_p\hat{x})\cdot z_\eta},$    (3.10)
            $u_s^{\infty,new}=u_s^\infty(\hat{x};d,d^\perp,\alpha,\beta,\Omega^{(e)})-u_s^\infty(\hat{x};d,d^\perp,\alpha,0,\widetilde{\Sigma}_j)\sum_{\eta=1}^{\eta_0}e^{\mathrm{i}(k_pd-k_s\hat{x})\cdot z_\eta}$
                $-u_p^\infty(\hat{x};d,d^\perp,0,\beta,\widetilde{\Sigma}_j)\sum_{\eta=1}^{\eta_0}e^{\mathrm{i}k_s(d-\hat{x})\cdot z_\eta},$    (3.11)
            $u^{\infty,new}=u_p^{\infty,new}+u_s^{\infty,new};$    (3.12)
Step 10 If $j=l''$, namely, the maximum number of the reference scatterers reaches, then stop the reconstruction; otherwise set $j=j+1$, and go to Step 6.
```

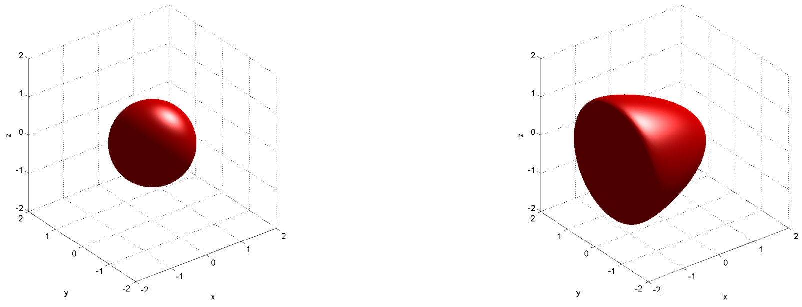

(a) (b)

Figure 3: Reconstructing multiple extended scatterers: base scatterer class.

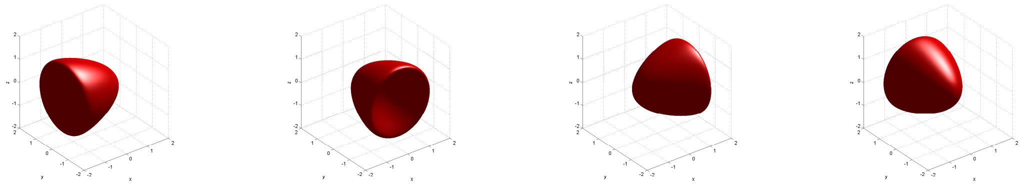

(a) (b) (c) (d)

Figure 4: Reconstructing multiple extended scatterers: the augmented 3D-kite. (a) the rotation degree is 0; (b) the rotation degree is 90; (c) the rotation degree is 180; (d) the rotation degree is 270.

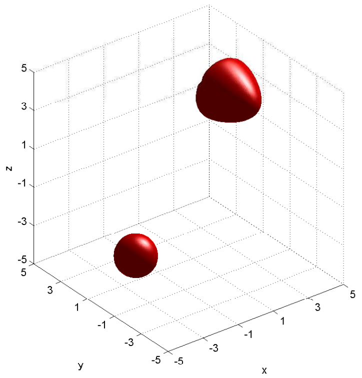

Figure 5: Reconstructing multiple extended scatterers: true scatterer

The 3D-kite is generated by revolving the 2D-kite lying in the plane $z=0$ around x-axis. For simplicity, the augmented data set is obtained by rotating the 3D-kite in the x-z plane every 90 degrees, see, e.g., the four orientations in Fig. 4, and by scaling the ball by one half, one and twice. For the located targets, we assume the multiple extended scatterers

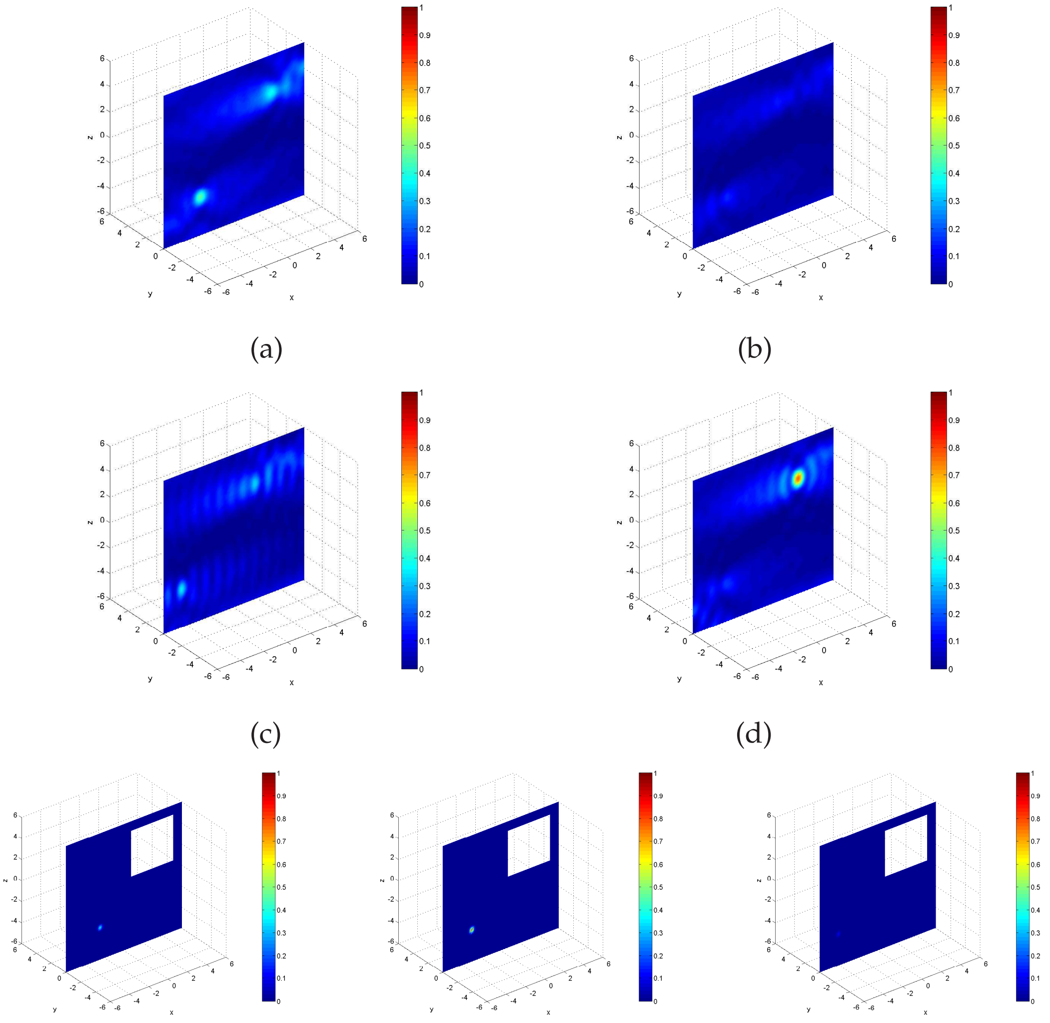

(a) (b)

(c) (d)

(e) (f) (g)

Figure 6: Reconstructing multiple extended scatterers: slice $y=0$ of W_2.

consist of two components. One of the components is a ball with radius 1 whose center lies at $(-3,0,-3)$; the other one is a 3D-kite with rotation 270 degree lying at $(3,0,3)$. The same as in Example 2.1, we set $\mu=1$ and $\lambda=2$. Moreover, in this example, we let the incident wave be of the form (1.1) with $\omega=2\pi$, $d=(1,0,0)$, $\alpha=1$ and $\beta=0$, and collect the needed far-field data on 590 Lebdev quadrature points for numerical integration.

We adopt W_1 to locate the regular-size scatterer components. By the increasing magnitude of the far field patterns, the Kite reference data is firstly employed for the locating purpose. Fig. 6(a)-(d) show that the first unknown component is a 3D-kite with rotation 270 degree, and the position of the 3D-kite is highlighted. One could find that, some

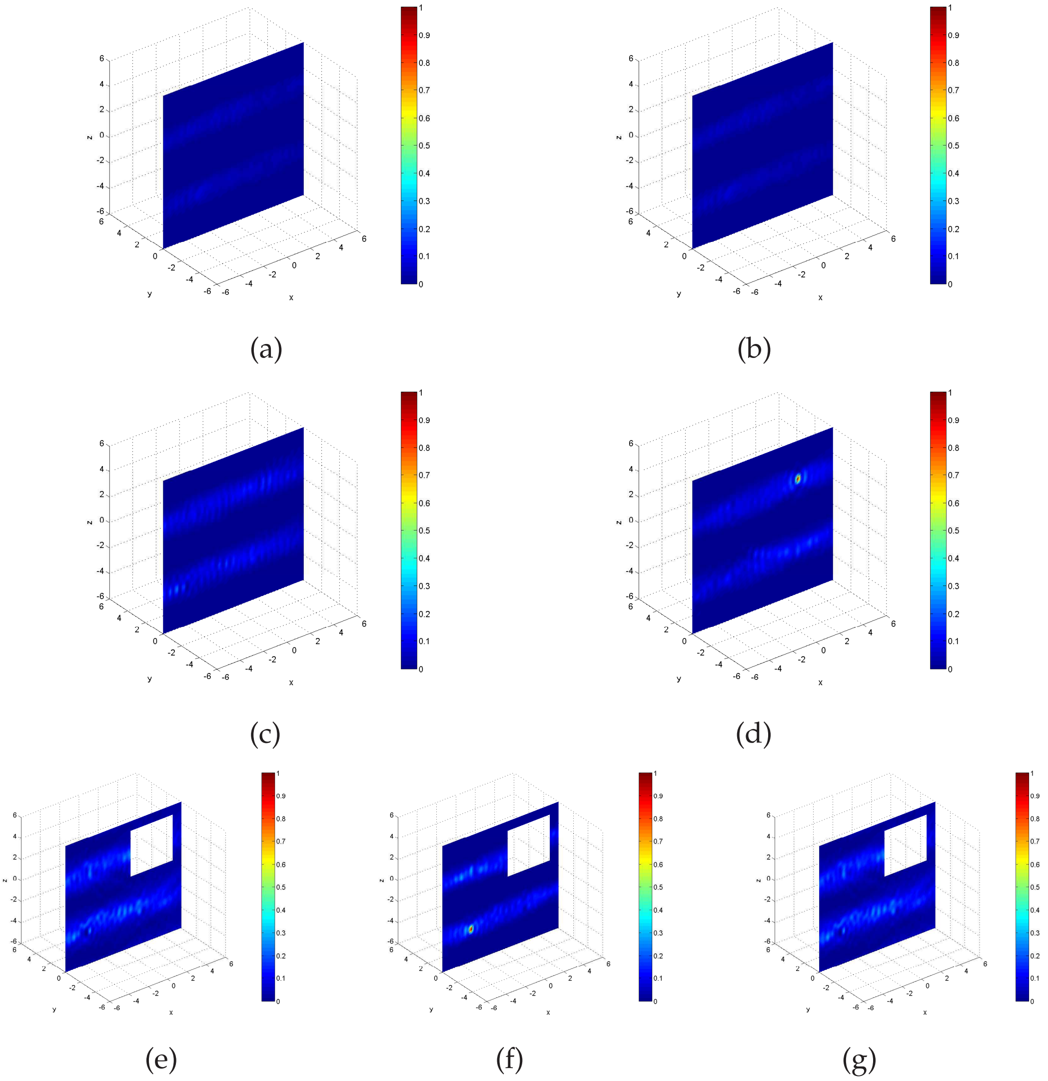

(a) (b)

(c) (d)

(e) (f) (g)

Figure 7: Reconstructing multiple extended scatterers: slice $y=0$ of W_2.

ghosts highlight close to the position of the ball in Fig. 6(a)-(d), which is largely due to the similarity between the far-field pattern of the two scatterer components. In the next stage, by subtracting the contribution of the 3D-kite from the total far-field data, we continue our reconstruction work with the far-field associated with the reference 3D-kite and its possible orientations. It is found in Fig. 6(e)-(g) that the most prominent indicating behavior identifies the size, shape and position of the ball. For comparison, Fig. 7 is also displayed to show the indicating behavior of W_2.

4 Reconstructing multiple multiscale scatterers

The elastic scatterer with multiscale components is of the following form

$$\Omega^{(m)} := \Omega^{(s)} \cup \Omega^{(e)}, \tag{4.1}$$

where $\Omega^{(s)}$ given in (2.3) and $\Omega^{(e)}$ given in (3.2) represent, respectively, the collections of small-size and regular-size scatterers. For $\Omega^{(m)}$ introduced above, we assume that $\operatorname{dist}(\Omega^{(s)} \cup \Omega^{(e)}) \gg 1$, which is also a technique consideration on reducing multiple scattering effect. Next, under the a priori knowledge that the base scatterer class $\mathcal{A}$ in (3.1) is known in advance, we consider how to recover the multiple multiscale scatterer components of $\Omega^{(m)}$.

The whole reconstruction procedure is a two-step process. More specifically, we shall adopt Algorithm 1 and Algorithm 2 to reconstruct the small and extended scatterer components, respectively. However, reconstructing the small components is really difficult, since the contribution of small scatterer components to the far-field patterns is too small to extract. Therefore, a *local tuning* technique is also incorporated in the second step of the multiscale reconstruction scheme. The exact definition of local tuning could be seen in [20]. In what follows, $\widehat{\Omega^{(e)}}$ is the reconstructed image of the extended scatterer $\Omega^{(e)}$, whereas $\widehat{\widehat{\Omega^{(e)}}}$ is an adjustment of $\widehat{\Omega^{(e)}}$ by locally adjusting the position, orientation and size of each component of $\widehat{\Omega^{(e)}}$. With these notations, we now formulate the scheme of reconstructing multiple multiscale scatterers in Algorithm 3.

In the following, we verify the multiscale scheme by a numerical example.

Example 4.1. Let the true scatterer be composed of a small rigid ball and a regular-size traction-free 3D-kite. The small ball is located at $(-3,0,0)$ whose radius is 0.1, and the 3D-kite is located at $(3,0,0)$ as shown in Fig. 8. We assume the augmented base scatterer class is the same with the one in Example 3.1. Let $\mu=1$, and $\lambda=2$, we detect the scatterer by impinging the incident wave with $\alpha=1$, $\beta=0$ and $\omega=2\pi$. In the following, we only present the results by using W_2 since it possesses better decaying properties.

First, we extract the information of the regular-size component using the indicator function $W_2(z)$ by computing the inner product with a priori known far-field data associated with those reference scatterer components with different orientations and sizes. We plot in Fig. 9(a)-(d) the indicator function values of $W_m(z)$ in one-to-one correspondence with the four orientations of the reference 3D-kite as shown in Fig. 4. It can be observed in Fig. 9(c) that the regular-size component in our locating target is the 3D-kite rotated by 180 degrees. Then we build a local tuning mesh to reconstruct the small components in the unknown multiscale scatterers. Fig. 9(g) shows that the small ball is located at $(-3,0,0)$; Meanwhile, from the results in Fig. 9(e)-(g), we could correct the position of the 3D-kite to be $(3,0,0)$.

Algorithm 3 Scheme for locating multiple multiscale scatterers $\Omega^{(m)}$

Step 1 For an unknown scatterer $\Omega^{(m)}$ with multiple components in (2.3), collect u_p^∞, u_s^∞ and u^∞ by sending a single detecting plane wave (1.1);

Step 2 Select a sampling region with a mesh $\mathcal{T}_h$ containing $\Omega^{(m)}$;

Step 3 Apply Algorithm 2 to reconstruct approximately the extended scatterer $\Omega^{(e)}$, denoted by $\widehat{\Omega^{(e)}}$;

Step 4 For $\widehat{\Omega^{(e)}}$ obtained above, select a local-tuning mesh $\mathcal{L}$;

Step 5 For a tune-up $\widehat{\widehat{\Omega^{(e)}}}$ relative to the local tuning mesh $\mathcal{L}$ calculate

$$\tilde{u}_\tau^\infty(\hat{x}) := u_\tau^\infty(\hat{x};\Omega^{(m)}) - u_\tau^\infty(\hat{x};,\widehat{\widehat{\Omega^{(e)}}}). \tag{4.2}$$

Apply Algorithm 1 with $\tilde{u}_\tau^\infty(\hat{x})$ as the far-field data to locate the significant local maximum points on $\mathcal{T}_h \backslash \mathcal{L}$;

Step 6 Repeat Step 5 by running through all the local tune-ups relative to $\mathcal{L}$. Locate the clustered local maximum points on $\mathcal{T}_h \backslash \mathcal{L}$, which correspond to the small scatterer components;

Step 7 Update $\widehat{\Omega^{(e)}}$ to the local tune-up $\widehat{\widehat{\Omega^{(e)}}}$ which generates the clustered local maximum points in Step 6.

5 Two-stage fast imaging of multiple multiscale scatterers

In this section, we consider to speed up the multiple multiscale imaging scheme. As can be observed in the numerical results in last section, one could get several bright spots by evaluating the indicator functions, which characterize the scatterer components. Since the decay of the spots is very fast, the locations we get are accurate. However, to capture the small spots, we have to take a rather fine grid, which brings us a huge computational cost, though most of the cost is spent on sampling in the irrelevant region (The region that is far away from all the scatterer components). Therefore, it is wise to trim most of the irrelevant region before evaluating the indicator values on the fine grid. In the following, we develop a two-stage strategy to realize this idea.

The coarse stage: coarse grid with u_p^∞

It has been analyzed in [25] that, the average decay radius of I_m or W_m around each center of the components is in inverse proportion to the wave number. Supposing $\lambda > 0$ and

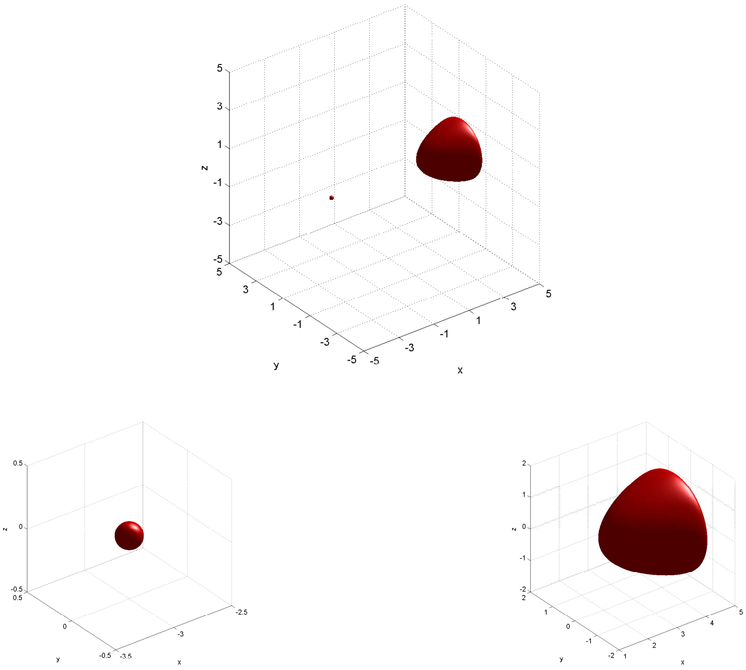

Figure 8: Reconstructing multiple multiscale scatterers: true scatterer.

recalling the fact that $k_s/k_p=\sqrt{(\lambda+2\mu)/\mu}$, we have $k_s>\sqrt{2}k_p$. Thus we could extract u_p^∞ from u^∞ and detect the unknown inclusions by evaluating I_1 or W_1. In light of the slow decay compared to I_1 or W_1, the corresponding spots posses larger radius, which enable us to take a coarse grid to capture the scatterer components.

The fine stage: fine grid with u_s^∞

In the fine stage, in order to extract the accurate information of the unknown bodies, we continue the reconstruction by using u_s^∞. That is, we first choose an appropriate threshold value. Comparing the values on the coarse mesh to the threshold value, we could further trim some irrelevant region and thus approach the locations of the scatterer components with I_2 or W_2.

We formulate the above two-stage multiscale sampling procedure in Algorithm 4. In the sequel, we present a numerical example to verify the effectiveness of the scheme proposed in Algorithm 4.

Example 5.1. The geometries considered in this example are composed of a 3D-kite and a regular tetrahedron, which are shown as in Fig. 10. The 3D-kite is located at $(0,3,3)$; the tetrahedron is located at $(0,-3,-3)$, and the side length of the tetrahedron is 0.1.

Algorithm 4 Scheme for the Two-stage Multiscale Reconstructing

```
Step 1  Determine the parameters: $H_0$, $h_0$, $c_1$, $c_2$;
Step 2  For the admissible reference scatterer class $\mathcal{A}$ in (3.1), formulate the augmented admissible $A_h$ in (3.6); collect in advance the P-part ($m=1$), S-part ($m=2$) or the full far-field data ($m=3$) associated with the admissible reference scatterer class $\mathcal{A}_h$ corresponding to a single incident plane wave of the form (1.1). Reorder $\mathcal{A}_h$ if necessary to make it satisfy assumption (ii), and also verify the generic assumption (i);
Step 3  For an unknown scatterer $\Omega^{(m)}$ in (3.2), collect the P-part, S-part or the full far-field data by sending the same detecting plane wave;
Step 4  Select a sampling region with a coarse mesh $\mathcal{T}_{H_0}$ containing $\Omega^{(m)}$;
Step 5  Set $j=1$;
Step 6  For each sampling point $z\in\mathcal{T}_{H_0}$, calculate $W_1^j(z)$ according to available far-field data for $\Omega^{(e)}$;
Step 7  Locate all those significant local maximum points of $W_1^j(z)$ satisfying $W_1^j(z)\approx 1$ for the scatterer components of the form $z+\widetilde{\Sigma}_j$. Let $z_\eta^{H_0}$, $\eta=1,\cdots,\eta_0$ be the local maximum points found in this step;
Step 8  For each $z_\eta^{H_0}$, find a cube $Cube(\eta,c_1)$ s.t., (i) $z_\eta^{H_0}\in Cube(\eta)$, (ii) for those nodes $z_j(j=1,2,\cdots,l_n)$ of the coarse mesh which are contained in $Cube(\eta)$, $W_1^j(z_j)>c_1$, (iii) For another cube $\widetilde{Cube(\eta)}$ which satisfies (i) and (ii), we have $Cube(\eta)\subset\widetilde{Cube(\eta)}$;
Step 9  Refine $\bigcup_{\eta=1}^{\eta_0} Cube(\eta)$ to obtain a fine mesh $\mathcal{T}_{h_0}^j$;
Step 10 Adopt the indicator $W_2^j$ on $\mathcal{T}_{h_0}^{\eta}$ to find $z_\eta^{h_0}$, $\eta=1,\cdots,\eta_0$ as the way stated in Step 6-7;
Step 11 Update the far-field patterns according to the formulae (3.10)-(3.12);
Step 12 If $j=l'$, namely, the maximum number of the reference scatterers reaches, then stop the reconstruction; otherwise set $j=j+1$, and go to Step 7.
Step 13 For $\widehat{\Omega^{(e)}}$ obtained above, select a local-tuning mesh $\mathcal{L}$;
Step 14 For a tune-up $\widehat{\widehat{\Omega^{(e)}}}$ relative to the local tuning mesh $\mathcal{L}$ calculate(4.2); Apply Algorithm 1 with $\tilde{u}_p^\infty(\hat{x})$ (Use $I_1(z)$) to locate the significant local maximum points on $\mathcal{T}_{H_0}\backslash\mathcal{L}$;
Step 15 Repeat Step 14 by running through all the local tune-ups relative to $\mathcal{L}$;
Step 16 Update $\widehat{\Omega^{(e)}}$ to the local tune-up $\widehat{\widehat{\Omega^{(e)}}}$, which generates the clustered local maximum points in Step 15; Let $\widetilde{z_\eta^{H_0}}(\eta=1,\cdots,\eta_1)$ denote the clustered local maximum points, build cube $Cube(\eta,c_2)$ around each $\widetilde{z_\eta^{H_0}}(\eta=1,\cdots,\eta_1)$;
Step 17 Refine $Cube(\eta,c_2)$ and correct the position of the small scatterers by implementing Algorithm 1 with $\tilde{u}_s^\infty(\hat{x})$ (Use $I_2(z)$) on the fine grid.
```

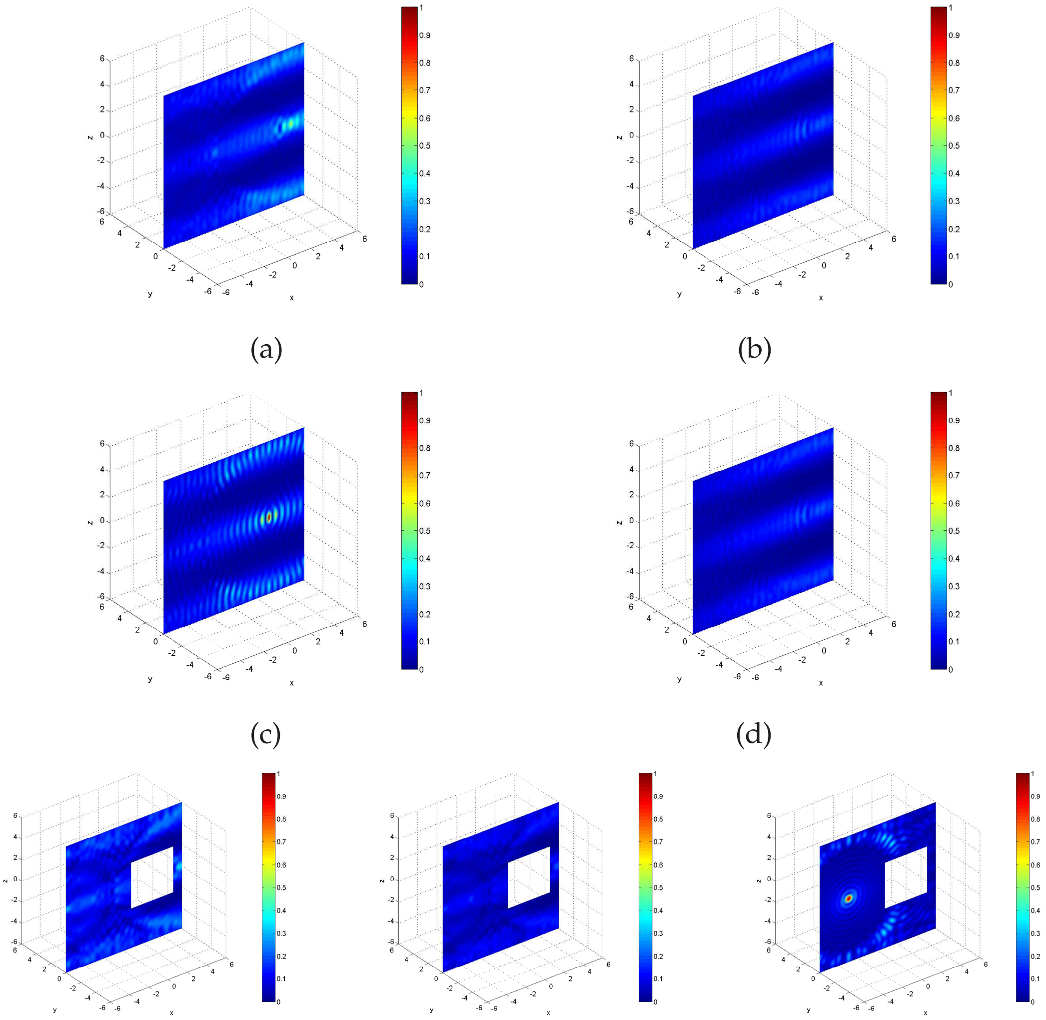

(a) (b)

(c) (d)

(e) (f) (g)

Figure 9: Reconstructing multiple multiscale scatterers: reconstruction result.

First, we adopt the low-frequency information, that is, we use W_1 to locate the extended component. In Fig. 11(a)-(b), we display the isosurface of $W_1=0.8$ when the right base far-field pattern (The far-field pattern of a 3D-kite with rotation 180 degrees) is chosen. From the theoretical analysis and inversion algorithms mentioned above, we could know that the center of the 3D-kite is surrounded in the isosurface. Then as stated in Algorithm 4, we properly choose a cube (see in Fig. 11(c)) covering the isosurface. Refine the cube (see in Fig. 11(d)) and continue the sampling process with W_2, we could get the values of the nodes on the fine grid. We display the isosurface $W_2=0.8$ in Fig. 11(e), from which a more accurate position information of the 3D-kite could be obtained. In

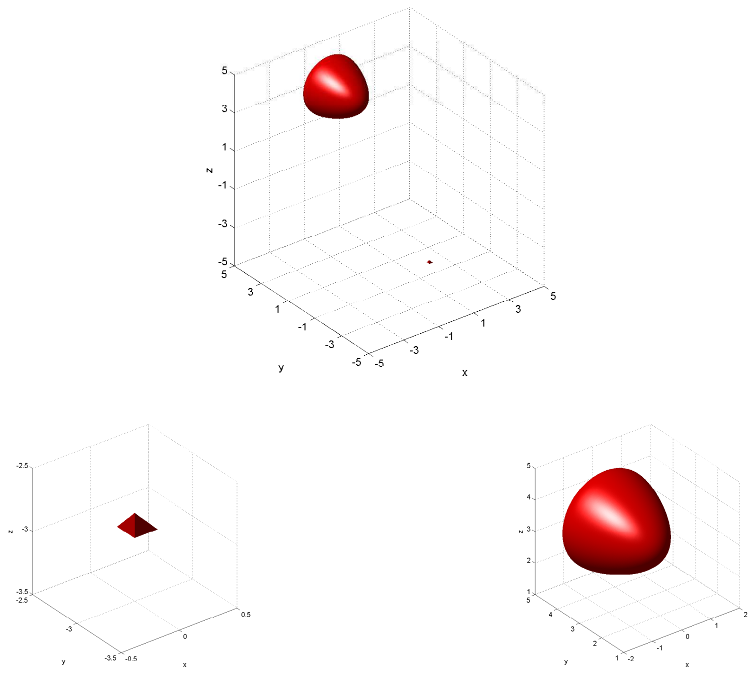

(b) (c)

Figure 10: Reconstructing multiscale scatterers with the two-stage sampling: true scatterer.

Fig. 11(g)-(h), we also display the slice $x=0$ of I_1 and I_2 when the contribution of the 3D-kite is properly subtract from the corresponding far-field pattern. Observing the bright spots in Fig. 11(g)-(h), we could find the necessity of two-stage sampling in the local tuning process, since the size of the bright spot is much smaller in Fig. 11(h).

Acknowledgments

This work was supported by the NSF of China (No. 11371115, 11201453, 91130022); the Shenzhen Research Program (No. JCYJ20140509143748226); FRG and Start-up Funds of Hong Kong Baptist University.

References

[1] I. Abubakar, *Scattering of plane elastic waves at rough surface I*, Proc. Cambridge Philos. Soc., **58** (1962), 136–157.

[2] C. Alves and H. Ammari, *Boundary integral formulae for the reconstruction of imperfections of small diameter in an elastic medium*, SIAM J. Appl. Math., **62** (2001), 503–531.

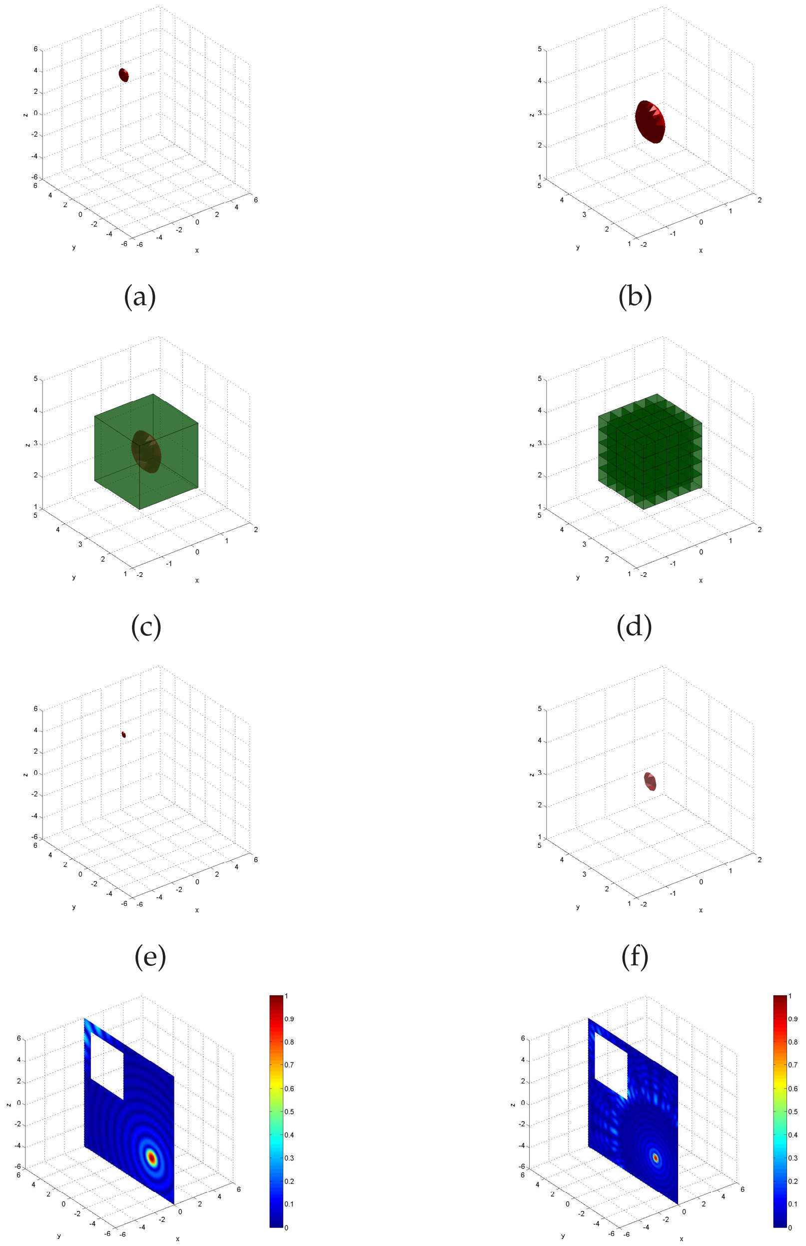

(a) (b)

(c) (d)

(e) (f)

(g) (h)

Figure 11: Reconstructing multiscale scatterers with the two-stage sampling: reconstruction results. (a) Sampling with W_1 on a coarse grid, where we display the isosurface of W_1 with value $c_1=0.8$; (b) Zoom in the result of (a); (c) Build a cube containing the red body; (d) Refine the cube to obtain a fine sampling grid; (e) Sampling with W_2 on a coarse grid, where we display the isosurface of W_2 with value $c_1=0.8$; (f) Zoom in of (e); (g) Sampling result with I_1 when the extended components are reconstructed correctly; (h) Sampling result with I_2 when the extended components are reconstructed correctly.

[3] H. Ammari, E. Bretin, J. Garnier, W. Jing, H. Kang, and A. Wahab, *Localization, stability, and resolution of topological derivative based imaging functionals in elasticity*, SIAM Journal on Imaging Sciences, **6** (2013), 2174–2212.

[4] H. Ammari, H. Kang, G. Nakamura, and K. Tanuma, *Complete asymptotic expansions of solutions of the system of elastostatics in the presence of an inclusion of small diameter and detection of an inclusion*, J. Elasticity, **67** (2002), 97–129.

[5] H. Ammari and H. Kang, *Polarization and moment tensors. With applications to inverse problems and effective medium theory*, Appl. Math. Sci., 162, Springer, New York, 2007.

[6] H. Ammari, H. Kang, and H. Lee,*Asymptotic expansions for eigenvalues of the Lamé system in the presence of small inclusions*, Comm. Part. Diff. Equ., 32 (2007), 1715–1736.

[7] C. J. Alves and R. Kress, *On the far-field operator in elastic obstacle scattering*, IMA J. Appl. Math., **67** (2002), 1–21.

[8] G. Bao, H. Y. Liu and J. Zou, *Nearly cloaking the full Maxwell equations: cloaking active contents with general conducting layers*, J. Math. Pures Appl., in press, 2013.

[9] R. Benites, K. Aki and K. Yomogida, *Multiple Scattering of SH waves in 2D media with many cavities*, Pageoph, **138** (1992), 353–390.

[10] D. P. Challa and M. Sini, *The Foldy-Lax approximation of the scattered waves by many small bodies for the Lame system*, arXiv: 1308.3072

[11] D. Colton and R. Kress, *Inverse Acoustic and Electromagnetic Scattering Theory*, 2nd Edition, Springer-Verlag, Berlin, 1998.

[12] J. Elschner and M. Yamamoto, *Uniqueness in inverse elastic scattering with finitely many incident waves*, Inverse Problems, **26** (2010), 045005.

[13] J. T. Fokkema, *Reflection and transmission of elastic waves by the spatially periodic interface between two solids (theory of the integral-equation method)*, Wave Motion, **2** (1980), 375–393.

[14] J. T. Fokkema and P. M. Van den Berg, *Elastodynamic diffraction by a periodic rough surface (stress-free boundary)*, J. Acoust. Soc. Am., **62** (1977), 1095–1101.

[15] D. Gintides and M. Sini, *Identification of obstacles using only the scattered P-waves or the Scattered S-waves*, Inverse Problems and Imaging, **6** (2012), 39–55.

[16] R. Griesmaier, *Multi-frequence orthogonality sampling for inverse obstacle scattering problems*, Inverse Problems, 27 (2001), 085005.

[17] P. Häner, G. C. Hsiao, *Uniqueness theorems in inverse obstacle scattering of elastic waves*, Inverse Problems, **9** (1993), 525–534.

[18] G. Hu, A. Kirsch and M. Sini, *Some inverse problems arising from elastic scattering by rigid obstacles*, Inverse Problems **29** (2013), 015009.

[19] G. Hu, J. Li and H. Liu, *Recovering complex elastic scatterers by a single far-field pattern*, J. Differential Equations, **257** (2014), 469–489.

[20] G. Hu, J. Li, H. Liu and H. Sun, *Inverse elastic scattering for multiscale rigid bodies with a single far-field pattern*, SIAM J. Imaging Sciences, **7** (2014), 1799–1825.

[21] G. C. Hsiao and W. L. Wendland, *Boundary Integral Equations*, Appl. Math. Sci., 164, Springer, Berlin Heidelberg, 2008.

[22] R. Kress, *Linear Integral Equations*, Berlin, Springer, 1989.

[23] V. D. Kupradze et al, *Three-dimensional Problems of the Mathematical Theory of Elasticity and Thermoelasticity*, Amsterdam, North-Holland, 1979.

[24] L.D. Landau, E.M. Lifshitz, *Theory of Elasticity*, Pergamon Press, 1986.

[25] J. Li and J. Zou, *A direct sampling method for inverse scattering using far-field data, Inverse Problems and Imaging*, **7** (2013), 757–775.

[26] H. Liu, *On near-cloak in acoustic scattering*, J. Differential Equations, **254** (2013), 1230–1246.

[27] H. Liu and H. Sun, *Enhanced near-cloak by FSH lining*, J. Math. Pures Appl., **99** (2013), 17–42.

[28] G. Nakamura and G. Uhlmann, *Identification of Lamé parameters by boundary measurements*, Amer. J. Math., **115** (1993), 1161–1187.

[29] G. Nakamura and G. Uhlmann, *Global uniqueness for an inverse boundary problem arising in elasticity*, Invent. Math., **118** (1994), 457–474. Erratum, **152** (2003), 205–207.

[30] G. Nakamura and G. Uhlmann, *Inverse problems at the boundary for an elastic medium*, SIAM J. Math. Anal., **26** (1995), 263–279.

[31] G. Nakamura, T. Kazumi and G. Uhlmann, *Layer stripping for a transversely isotropic elastic medium*, SIAM J. Appl. Math., **59** (1999), 1879–1891.

[32] L. V. Rachele, *Uniqueness of the density in an inverse problem for isotropic elastodynamics*, Trans. Amer. Math. Soc., **355** (2003), 4781–4806.

[33] J. W. C. Sherwood, *Elastic wave propagation in a semi-infinite solid medium*, Proc. Phys. Soc., **71** 1958, 207–219.